RESEARCH ARTICLE

ADVANCED MATERIALS
www.advmat.de

Unlocking the Ambient Temperature Effect on FA-Based Perovskites Crystallization by In Situ Optical Method

*Yunfan Wang, Zixin Zeng, Yuxuan Zhang, Zhuoqiong Zhang, Leyu Bi, Aoxi He, Yuanhang Cheng, Alex K.-Y. Jen, Johnny C. Ho, and Sai-Wing Tsang**

Multiple cation-composited perovskites are demonstrated as a promising approach to improving the performance and stability of perovskite solar cells (PSCs). However, recipes developed for fabricating high-performance perovskites in laboratories are always not transferable in large-scale production, as perovskite crystallization is highly sensitive to processing conditions. Here, using an in situ optical method, the ambient temperature effect on the crystallization process in multiple cation-composited perovskites is investigated. It is found that the typical solvent-coordinated intermediate phase in methylammonium lead iodide ($MAPbI_3$) is absent in formamidinium lead iodide ($FAPbI_3$), and nucleation is almost completed in $FAPbI_3$ right after spin-coating. Interestingly, it is found that there is noticeable nuclei aggregation in Formamidinium (FA)-based perovskites even during the spin-coating process, which is usually only observed during the annealing in $MAPbI_3$. Such aggregation is further promoted at a higher ambient temperature or in higher FA content. Instead of the general belief of stress release-induced crack formation, it is proposed that the origin of the cracks in FA-based perovskites is due to the aggregation-induced solute depletion effect. This work reveals the limiting factors for achieving high-quality FA-based perovskite films and helps to unlock the existing narrow processing window for future large-scale production.

1. Introduction

Metal halide perovskite is fast becoming a crucial component in photovoltaic technology due to its excellent photoelectric properties, such as high optical absorption, prolonged charge carrier lifetime, and facile bandgap tuning. The power conversion efficiency (PCE) of PSCs has increased from 3.8% to 26.1% since it was first reported in 2009.[4] Among various perovskite materials, $FAPbI_3$ perovskite demonstrates excellent potential to be an ideal candidate for high-efficiency single junction PSCs owning to its desirable bandgap (1.48 eV), as deduced from the Shockley–Queisser limit.[1a] However, compared to MA-based perovskite, it is well known that the large size of FA cations leads to perovskite phase instability in pure $FAPbI_3$, which causes the PbI_6^{4-} framework unstable and induces phase transition from photovoltaic active α-$FAPbI_3$ (cubic) phase to inactive δ-$FAPbI_3$ (hexagonal) phase.[5] Previous studies have proposed that adding small-size cations can effectively suppress the phase transition by modulating the average cation size. Therefore, the utilization of mixed cation-composited perovskite has become a common tactic to improve the device performance and stability. In particular, Bein et al. have found that a mixture of MAI and FAI can suppress the lattice expansion induced by FA cations, and the stronger interactions between PbI_6^{4-} framework and MA cations can also stabilize the perovskite lattice.[1b] Recently, based on this strategy, Liu and co-workers obtained a device exhibiting a champion PCE of 24.29%, one of the highest values reported for FAMA-based PSCs.[4c] The devices also

---

Y. Wang, Z. Zeng, Y. Zhang, A. K.-Y. Jen, J. C. Ho, S.-W. Tsang
Department of Materials Science and Engineering
City University of Hong Kong
Hong Kong, Hong Kong SAR 999077, China
E-mail: saitsang@cityu.edu.hk

Z. Zhang
Department of Physics and Institute of Advanced Materials
Hong Kong Baptist University
Hong Kong, Hong Kong SAR 999077, China

L. Bi, A. K.-Y. Jen
Department of Chemistry
City University of Hong Kong
Hong Kong, Hong Kong SAR 999077, China

The ORCID identification number(s) for the author(s) of this article can be found under https://doi.org/10.1002/adma.202307635

DOI: 10.1002/adma.202307635

A. He
College of Materials Science and Engineering and Institute of New Energy and Low-carbon Technology
Sichuan University
Chengdu 610064, P. R. China

Y. Cheng
School of New Energy
Nanjing University of Science and Technology
Jiangyin, Jiangsu 21443, China

A. K.-Y. Jen, S.-W. Tsang
Center of Super-Diamond and Advanced Films (COSDAF)
and Hong Kong Institute for Clean Energy
City University of Hong Kong
Hong Kong, Hong Kong SAR 999077, China

presented excellent long-term phase stability even after being exposed to air for more than 1000 h.

Nonetheless, the quality of the FAMA-based perovskites is highly susceptible to the fabrication conditions, such as ambient temperature, antisolvent usage, and even the atmosphere within the glovebox.[6] This poses a threat to large-scale production, which requires very high reliability. Interestingly, Saliba et al. have demonstrated that the PCE of the device is significantly reduced when the perovskite films are fabricated above 27 °C inside a glovebox.[7] Similarly, Ye et al. have also mentioned that the performance of $FA_{0.85}MA_{0.15}Pb(I_{0.85}Br_{0.15})_3$ PSCs fabricated in winter is much better than that in summer due to cracks formation.[8] To solve this problem, the authors regulated the processing temperature by a cooling system during the spin-coating of the perovskite film. By regulating the temperature from 32 to 18 °C, the PCE was significantly increased from 13% to 18%. Although cooling can improve the FAMA-based perovskite performance effectively, it increases the production cost and reduces the competitiveness in the market. Hence, it is critical to seek alternatives that can increase the processing window. However, the intrinsic mechanism of such temperature effect on the film quality still remains elusive.

Recently, Wang et al. observed noticeable cracks on $FA_{0.87}MA_{0.13}Pb(IBr)_3$ films and ascribed that to stress release induced by rapid crystal growth. Introducing methylammonium chloride into the precursor solution can effectively slow down the crystallization process and achieve crack-free films with a mirror-like surface.[3b] In addition, Lee et al. have demonstrated that mixing the ethyl acetate and hexane as the antisolvent can also regulate the crystal growth and passivate the grain boundary located in the crack regions.[9] Besides, Li et al. have reported a liquid medium annealing method that provides a robust chemical environment to modulate the crystallization. This method is less dependent on the fabrication environment and the fabricated devices show little performance variation over a year.[10] In addition, Feng et al. introduced a simple preseeding strategy with the incorporation of perovskite-phase $MAPbI_3$ microcrystals into $FAPbI_3$ perovskite precursors to alter the size of colloid particles in the precursor solution. This approach increases the nucleation rate and suppresses the crystallization of perovskite, resulting in high-quality perovskite films. Based on this strategy, the authors obtained a device with a champion PCE of 24.31%.[11] Although many previous studies have underscored the importance of controlling the fast crystallization in mixed cation perovskites for achieving high-efficiency devices, the underlying microscale mechanisms governing the phase evolution during the crystallization have yet to be conclusively defined.[12] It is mainly because there is a lack of valid experimental approaches to monitoring the rapid crystallization process, which hinders the transformation from laboratory to large-scale production.

In this work, we investigated the impacts of ambient temperature effect on the crystallization process of $FA_xMA_{1-x}PbI_3$ perovskites by in situ optical techniques. Prototypical $MAPbI_3$ and $FAPbI_3$ were used as reference material systems to identify the different growth mechanisms contributed by the two different cations. Combining DFT results, it is found that pure $MAPbI_3$ tends to form a solvent-combined phase, while pure $FAPbI_3$ tends to form the δ-perovskite phase during spin-coating. In mixed cation $FA_xMA_{1-x}PbI_3$ perovskites, we have found that the $FAPbI_3$ framework is first generated, followed by the incorporation of MA ions into the crystal lattice. We have found that the crystallization is very sensitive to both the FA content and the ambient temperature. The higher FA content and elevated ambient temperature significantly decrease the amount of residual solvent, suppressing the formation of the solvent-combined intermediate phase. As a result, due to the lack of hindrance from the solvent adducts, crystallization occurs spontaneously during the spin-coating and competes with the nucleation process, resulting in rough and nonuniform perovskite films. Consequently, it leads to the crack formation. Overall, this work provides a unique and intuitive perspective toward the understanding of the FAMA-based perovskite growth mechanism.

2. Results and Discussion

2.1. Ambient Temperature Effect on $FAMAPbI_3$ Perovskite Films and Solar Cells

We noticed that the performance of FAMA-based PSCs is strongly dependent on the ambient temperature. **Figure 1**a shows the current-voltage (J–V) characteristics under 100 mW cm^{-2} AM 1.5G illumination of $MAPbI_3$ and $FA_{0.5}MA_{0.5}PbI_3$ PSCs with perovskite films fabricated at 22 and 30 °C, the corresponding photovoltaic parameters are summarized in Table S1 of the Supporting Information. For $MAPbI_3$, the devices fabricated at the two ambient temperatures show comparable performance. However, the performance of $FA_{0.5}MA_{0.5}PbI_3$ PSCs is significantly different. Particularly, the open-circuit voltage (V_{OC}) is reduced from 1.15 to 1.09 V, and the fill factor (FF) is reduced from 79.2% to 69.6% when the ambient temperature is increased from 22 to 30 °C. Generally, V_{OC} and FF are strongly affected by the defect density in the perovskite films (as shown in Figure S3, Supporting Information), which is directly related to the film morphology.[13] In addition, analysis of the statistical device performance (Figure S4, Supporting Information) reveals that $FA_{0.5}MA_{0.5}PbI_3$ devices exhibit poorer repeatability than $MAPbI_3$ at a higher ambient temperature, suggesting that the $FA_{0.5}MA_{0.5}PbI_3$ film quality is more sensitive to the processing conditions.

To better understand the impacts of the ambient temperature effect on perovskite film quality, we controlled the glovebox temperature using a refrigerating system and fabricated the perovskite films at a series of ambient temperatures (from 18 to 30 °C). The devices performance with the perovskite films fabricated at the ambient temperature below 22 °C is comparable (Figure S6, Supporting Information).

Figure 1c shows the digital images of the as-cast and annealed $FA_{0.5}MA_{0.5}PbI_3$ films fabricated at different ambient temperatures. It is worth noting that the $FA_{0.5}MA_{0.5}PbI_3$ film fabricated at around the room temperature of 26 °C already exhibits a rough surface with multiple cracks right after the spin-coating. This is consistent with the corresponding scanning electron microscope (SEM) shown in (Figure S7, Supporting Information). Those features are also replicated after the thermal annealing (120 °C, 40 min). On the other hand, a smooth and mirror-like surface was observed for the film fabricated at 22 °C or below. According to previous studies, the formation of cracks is ascribed to the lattice

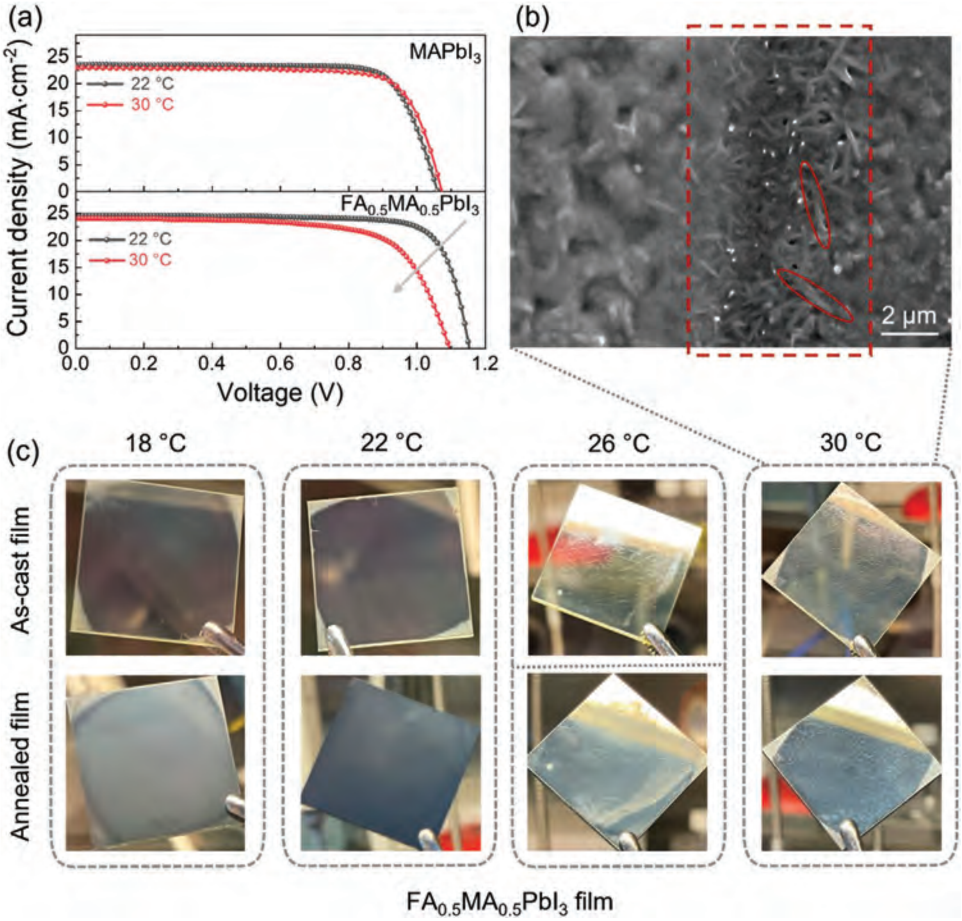

Figure 1. a) The *J*–*V* curves of MAPbI$_3$ and FA$_{0.5}$MA$_{0.5}$PbI$_3$-based PSCs fabricated at different ambient temperatures. b) The SEM image of the as-cast FA$_{0.5}$MA$_{0.5}$PbI$_3$ perovskite film fabricated at an ambient temperature of 30 °C. c) The digital images of as-cast and annealed FA$_{0.5}$MA$_{0.5}$PbI$_3$ perovskite films fabricated at series ambient temperatures (from 18 to 30 °C).

stress release caused by the fast crystallization in FA-based perovskite. In such a case, it is expected that the crack region should be a void region surrounded by large crystal gains. However, the profilometer test results indicate that the crack region still has a thickness of ≈60 nm. In addition, the SEM image (Figure 1b) of the as-casted film fabricated at 30 °C further shows that there are needle-shaped grains residual in the crack region. On both sides of the crack, there are clusters of small gains instead of large crystals. Hence, the crack formation is more likely due to the aggregation of the small gains during the spin-coating process. To get more insight into the grain aggregation in the crack region, we conducted photoluminescence (PL) imaging on the annealed perovskite films. The PL peak position mapping image (Figure S8a, Supporting Information) shows that the crack region has longer wavelength emission, indicating the FA-rich phases with a smaller bandgap. In addition, the PL full width at the half maximum mapping (Figure S8b, Supporting Information) further indicates that the FA-rich phases in the crack region exhibit poorer homogeneity. Besides the cracks, further analysis of the SEM and atomic force microscopy (AFM) images (Figure S9, Supporting Information) reveals that the FA$_{0.5}$MA$_{0.5}$PbI$_3$ film fabricated at 30 °C has more than two times increase in surface roughness.

According to the above results, it can be confirmed that the significant difference in device performance with the FA$_{0.5}$MA$_{0.5}$PbI$_3$ films prepared at 22 and 30 °C is attributed to the distinctive surface morphology right after the spin-coating. In particular, there are a large number of cracks with a width of more than 5 μm distributed in the film fabricated at 30 °C. Although no large crystals have yet been formed, the small gains in the film tend to aggregate and induce cracks. The crack formation seems to be a detrimental factor leading to poor device performance, but it is still unclear the origin of the crack formation. It has been widely ascribed to the stress release during the growth of the crystal.[3,14] However, according to the SEM and profilometer results, those cracks have already been formed right after the spin-coating before any large crystals have been developed, where the films are mainly composited with small perovskite gains. Hence, such crack formation may be more likely due to the gain aggregation in the crystallization process during spin-coating. To better understand the phase evolution of the perovskite film after the spin-coating, we conducted the X-ray diffraction (XRD), UV–vis absorption, and PL measurements of the as-cast perovskite films, as summarized in Figure S10 of the Supporting Information. The results suggest that α-phase perovskite has already been formed in spin-coating at an ambient temperature of 30 °C, which is absent in the film prepared at 22 °C. It is worth noting that the as-casted $FA_{0.5}MA_{0.5}PbI_3$ film is metastable, which is very sensitive to exposure to the environment, especially during the sample transfer and the measurement. Therefore, the in situ technique would provide a more qualitative analysis of the details of the crystallization process.

2.2. In Situ Optical Study on Single Cation Perovskite Crystallization

We sought to investigate in detail the nucleation and crystallization in $FAMAPbI_3$ using the in situ optical techniques during the spin-coating and annealing processes. The schematic diagram of the in situ optical measure system is shown in Figure S11 of the Supporting Information, which is integrated with the spin-coating and thermal annealing processes inside a nitrogen-filled glovebox. A laser excitation source (λ_{ex} = 450 nm, 8 mW cm^{-2}) was used for the in situ PL test, and a halogen lamp was used as the light source for the in situ absorption test. In order to better understand the correlation between the in situ results and the crystallization in mixed cations perovskite, it is essential to establish such correlation in individual single cation perovskites of $MAPbI_3$ and $FAPbI_3$.

2.2.1. $MAPbI_3$ Perovskite

The in situ optical spectra evolution of the $MAPbI_3$ perovskite precursor films is presented in **Figure 2**a–e, which can be divided into four stages. The 0 s in the x-axis corresponds to the time of dropping the antisolvent.

Stage I: Supersaturation-induced nucleation

Upon dropping the antisolvent, the PL signal is detected with increasing intensity with time, and the PL peak position is rapidly shifted from 740 to 755 nm. At this stage, nucleation is triggered by the antisolvent, by effectively increasing the solute concentration. The shorter wavelength emission at the beginning is due to the quantum confinement effect.[15] Meanwhile, the increase in optical absorption due to the nucleation can also be observed.

Stage II: Nuclei redissolution and formation intermediate phase

The PL and absorption intensities decrease rapidly to the noise level within 2 s. Previous studies have associated this phenomenon with the formation of a nonradiative solvent-combined phase.[6b,16] In this experiment, a mixture of solvents was prepared by combining 850 µL dimethylformamide (DMF) with 150 µL dimethyl sulfoxide (DMSO), which were widely reported for achieving high-efficiency PSCs. Due to the lower vapor pressure and higher boiling point of DMSO, it is hard to be removed by the antisolvent.[17] Consequently, the residual DMSO in the wet film redissolves the nuclei and forms the MAI–DMSO–PbI_2 intermediate phase, which is supported by the XRD result of the as-cast $MAPbI_3$ film (Figure S15a, Supporting Information). The weak PL signal after the rapid drop also suggests that some large grains, which have longer wavelength emission are also formed at this stage. Owning to the lower surface energy, they are more difficult to be dissolved by the residual DMSO.

Stage III: Secondary nucleation and crystallization

Subsequently, after the sample was transferred to a hotplate for annealing at 120 °C, distinct changes in PL and absorption signals are detected at ≈10 s, as shown in Figure 2d. According to the temperature evolution of the sample measured by an infrared camera (Figure S16, Supporting Information), the temperature on the sample surface rapidly increases to ≈80 °C in 10 s. At this temperature, it provides enough thermal energy to accelerate the solvent evaporation and promote the secondary nucleation. It is also supported by the strong absorption signal by the small nuclei observed at ≈450 nm (red circle in Figure 2d). Consequently, this secondary nucleation increases the number of the small nuclei, causing a blueshift (red circle in Figure 2e) of the PL peak position from 758 to 737 nm. Furthermore, the secondary nucleation largely enhances the PL intensity which reaches a maximum at ≈25 s (indicated by the blue circle in Figure 2e). After that, crystallization occurs and the perovskite phase is becoming more established, as indicated by the increasing optical absorption toward the desired band edge (760 nm). On the other hand, there is a sharp decrease in PL intensity due to the thermal quenching effect (see Figure S17, Supporting Information).[16,18]

Stage IV: Formation of bulk $MAPbI_3$

After 50 s, it is evident that the PL signals continue to become narrower at a relatively consistent peak position, and the absorption edge becomes clear and remains at the same value, indicating the formation of the bulk perovskite phase. During the annealing process, the PL peak position is increased from 756 to 778 nm, suggesting an increase in the size of the $MAPbI_3$ crystals.

2.2.2. $FAPbI_3$ Perovskite

The in situ optical spectra evolution of the $FAPbI_3$ perovskite precursor films is presented in Figure 2f–j, which can also be divided into four stages.

Stage I: Nucleation

The temporal evolution of the PL and absorption are similar to that in $MAPbI_3$ as discussed above, but those in stages II to IV are significantly different.

Stage II: Transformation from α to δ-phase perovskite

At this stage, the PL intensity in the $FAPbI_3$ also decreases but the rate is slower than that in $MAPbI_3$. Since the interaction between FA and DMSO is weaker than that between MA and DMSO, it rules out the possibility of redissolution of the nuclei as in $MAPbI_3$. On the other hand, the α-phase $FAPbI_3$ is unstable which will gradually convert to the more thermodynamically stable δ-phase. The δ-$FAPbI_3$ is photovoltaic inactive and nonluminous. Therefore, such a gradual phase transformation leads to a slow decrease in PL intensity. It is supported by the XRD result of the as-cast $FAPbI_3$ film, as shown in Figure S15b of the Supporting Information.[19] In addition, the intensity of the δ-phase diffraction peak is very high, suggesting large aggregates of δ-phase perovskite are already formed during the spin-coating, which is consistent with the SEM results as shown in Figure S18 of the Supporting Information. However, δ-phase perovskite is nonradiative (indirect bandgap) with an optical absorption band edge shorter than 500 nm, which cannot be detected by the in situ PL and absorption measurement.[20]

Stage III and IV: Transformation from δ to α-phase and formation of bulk crystals

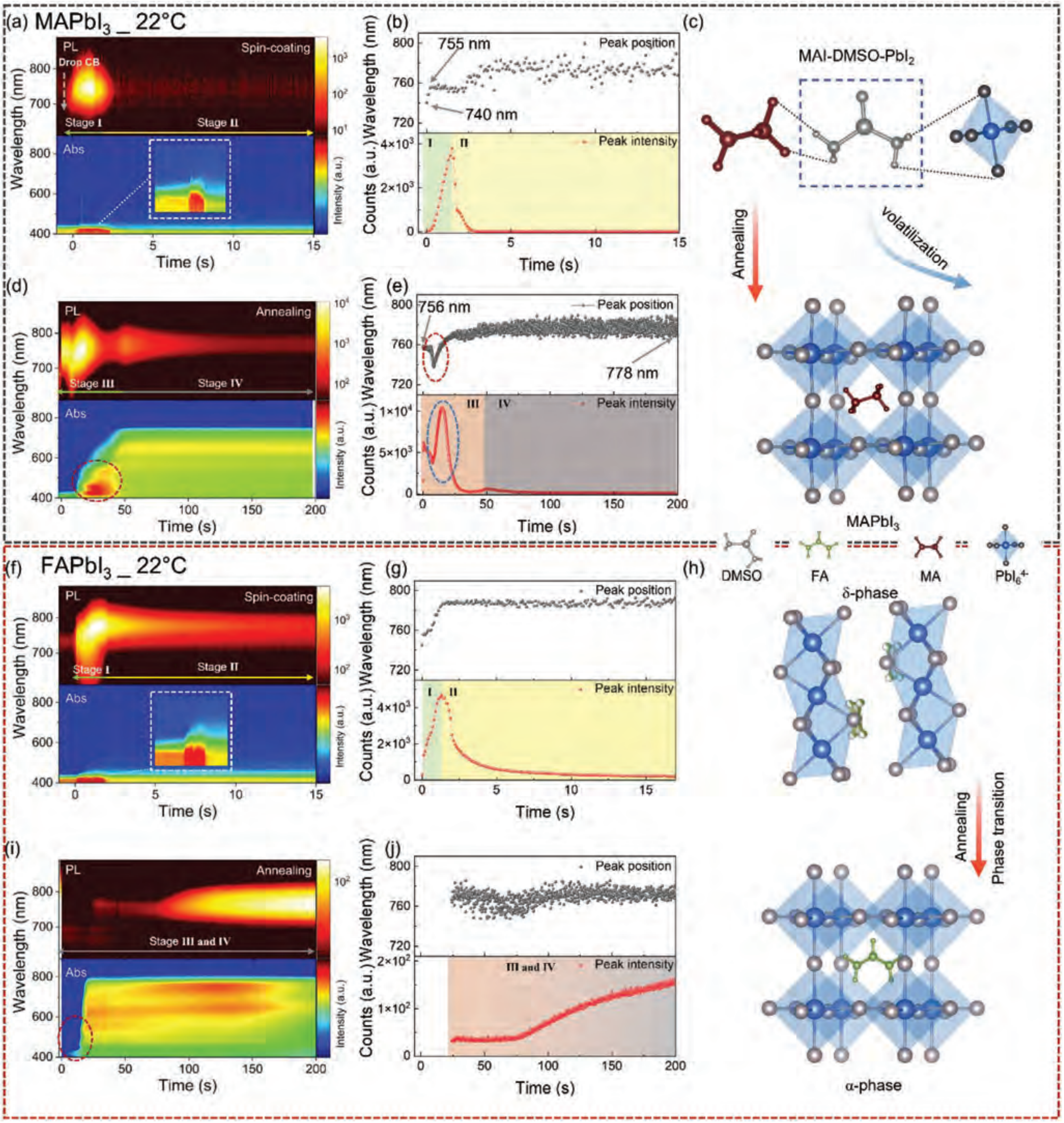

Figure 2. The in situ PL and absorption evolution of $MAPbI_3$ during a) spin-coating and d) annealing. The extracted evolution of the PL peak position and intensity by Gaussian fitting during b) spin-coating and e) annealing. c) The schematic diagram of the $MAPbI_3$ crystallization process. The in situ PL and absorption evolution of $FAPbI_3$ during f) spin-coating and i) annealing. The extracted evolution of PL peak position and intensity by Gaussian fitting during g) spin-coating and j) annealing. h) The schematic diagram of the $FAPbI_3$ crystallization process.

During annealing, no PL signal is detected until after 25 s, which is attributed to the fact that the as-cast film is dominant by the nonluminous δ-phase. Until the δ-phase obtains enough thermal energy in annealing, it will transfer back to α-$FAPbI_3$, resulting in an increase of the PL signal.[19] Surprisingly, a very steep increase in absorption (red circle in Figure 2i) is observed at ≈10 s. Compared to $MAPbI_3$, where the absorption has a gradual increase during the first 20 to 30 s, the abrupt increase in absorption toward the desired bandgap suggests that most gains in $FAPbI_3$ are already formed and aggregated before annealing. The thermal energy can readily facilitate the transformation of the δ-phase to the α-phase $FAPbI_3$. It is also consistent with the above intense δ-phase observed in the XRD results. In addition, no secondary nucleation signal is detected at the beginning of the annealing that is observed in $MAPbI_3$, indicating that the nucleation has been mostly completed in $FAPbI_3$ during the spin-coating. As mentioned, the secondary nucleation arises from the DMSO-combined phase in $MAPbI_3$. Hence, it suggests that only a small amount of DMSO is residual in the as-cast $FAPbI_3$ film. After 70 s, the PL intensity increases gradually, but the absolute PL counts are much smaller than that in $MAPbI_3$. Such an increase in PL intensity can be ascribed to continuous phase transition or the decrease of defect density during the crystal growth.[19,21] The overall low intensity is due to the influence of the thermal quenching effect, as discussed above.

Based on the above in situ PL and absorption results of the two single cation perovskites, the crystallization process of $MAPbI_3$ and $FAPbI_3$ perovskite films are illustrated in Figure 2c,h. For $MAPbI_3$, the MAI–DMSO–PbI_2 intermediate phase is formed during the spin-coating, which retards the further nucleation or crystallization until the residual DMSO is evaporated in the thermal annealing process. On the other hand, the nucleation in $FAPbI_3$ is more efficient, which continues to grow and aggregate due to the absence of the FAI–DMSO–PbI_2 intermediate phase, and the initially formed α-phase is immediately converted to the more stable δ-phase. However, the large amount of aggregation during the spin-coating is detrimental to the resulting film morphology, leading to the formation of rough $FAPbI_3$ film with multiple cracks, as shown in Figure S19 of the Supporting Information.

2.3. In Situ Optical Study on Mixed Cation Perovskite Crystallization

Having the correlation between the in situ results and the corresponding crystallization in the reference systems of $MAPbI_3$ and $FAPbI_3$, we further investigated the crystallization kinetics of the $FA_xMA_{1-x}PbI_3$ perovskite during the spin-coating and annealing processes. In order to prevent the optical signal from being obscured by the phase transition in perovskite with high FA content ($x > 50$) (Figure S20, Supporting Information), we first prepared the perovskite with a low concentration of FA (25%).

The in situ optical spectra evolution of the $FA_{0.25}MA_{0.75}PbI_3$ perovskite precursor film fabricated at an ambient temperature of 22 °C (FA-25_22) is shown in **Figure 3**a–e. The temporal evolutions of the PL and absorption in Stage I are similar to that in $MAPbI_3$ and $FAPbI_3$. However, a totally different Stage II in the FA-25_22 film is observed. As mentioned, the PL intensity for single cation perovskites sharply decreases in Stage II, which is ascribed to the formation of the DMSO adduct phase in $MAPbI_3$ or δ-phase in $FAPbI_3$. Interestingly, there is a continuous gradual increase of PL intensity for the FA-25_22 film, and it is attributed to smaller size MA cations which stabilize the $PbI_6{}^{4-}$ framework in α-phase $FAMAPbI_3$. As a result, the α-phase $FAMAPbI_3$ can continue to grow, as supported by the continuous red-shifting in PL peak position from 775 to 783 nm during Stage II (Figure 3b).[15d] Moreover, the FA cations reduce the amount of the residual solvent in the FA-25_22 film during the spin-coating, thereby preventing the perovskite nuclei from redissolution. Overall, the increase in PL intensity is related to the luminated nuclei growth, which is further supported by the slightly enhanced absorption intensity (Figure 3a).

After 20 s of annealing, the increase in absorption signal at ≈500 nm (red circle in Figure 3d) and the subtle increase in PL intensity (blue circle in Figure 3e) suggest that there is a small amount of secondary nucleation. After that, the bulk perovskite phase starts to form, indicated by the increasing optical absorption towards the desired band edge (780 nm).

2.3.1. Ambient Temperature Effect

Figure 3f–i shows the optical spectra evolution of the FA-25 film fabricated at 30 °C (FA-25_30). During spin-coating, the temporal PL signal is comparable to that in the FA-25_22 film. However, a secondary increase of absorption intensity toward the longer wavelength is observed in the FA-25_30 film after 5 s of spin-coating (Figure 3f), indicating there is a certain degree of nuclei aggregation. As demonstrated above, the nucleation in $FAPbI_3$ is more efficient than that in $MAPbI_3$. The FA-based perovskite generally has a high density of nuclei formed during the spin-coating process. This increases the probability of nuclei aggregation. It is worth noting that, during spin-coating, the perovskite film is in the form of a solid-solution thin film, and the separation of the nuclei is determined by the amount of the residual solvent. Consequently, it can be easily understood that at a higher temperature, as the solvent evaporation rate increases, the reduced amount of the residual solvent increases the probability of nuclei aggregation. More importantly, as the wet film has a larger volume than a dry film, a large amount of nuclei aggregation in a wet film can induce solute depletion in certain regions.[22] It is consistent with the crack-like morphology observed in the FA-based perovskite films. In addition, instead of a void region that is generally expected in cracks due to the stress release of the crystal plane, there is still a considerable amount of material in the FA-based perovskite cracks.

According to the above results, the crystallization evolution in the mixed cation perovskite is illustrated in Figure 3c. After dropping antisolvent, the $FAPbI_3$ framework is first generated, which is then followed by the incorporation of MA, resulting in the blue shift of the PL peak position. The MA ions stabilize the α-$FAPbI_3$ phases and suppress the δ-$FAPbI_3$ phase formation, resulting in persistent α-$FAPbI_3$ nuclei growth. At a higher ambient temperature, it increases the evaporation rate of the residual solvent, further prompting the nuclei growth and inducing the nuclei aggregation.

2.3.2. In Higher FA Content

To confirm the effect of the FA cations on the crystallization process, we further increased the FA concentration to 50% in the mixed cation perovskite and conducted the in situ measurement. As shown in **Figure 4**. The in situ results in $FA_{0.5}MA_{0.5}PbI_3$ film fabricated at 30 °C (FA-50_30) resemble that in the FA-25_30 film. A fast nucleation process starts upon dropping the antisolvent, and the PL peak position reaches the bulk emission at ≈780 nm in less than 2 s, indicating the aggregation of nuclei is stronger in FA-50_30 than that in FA-25_30. This is supported by

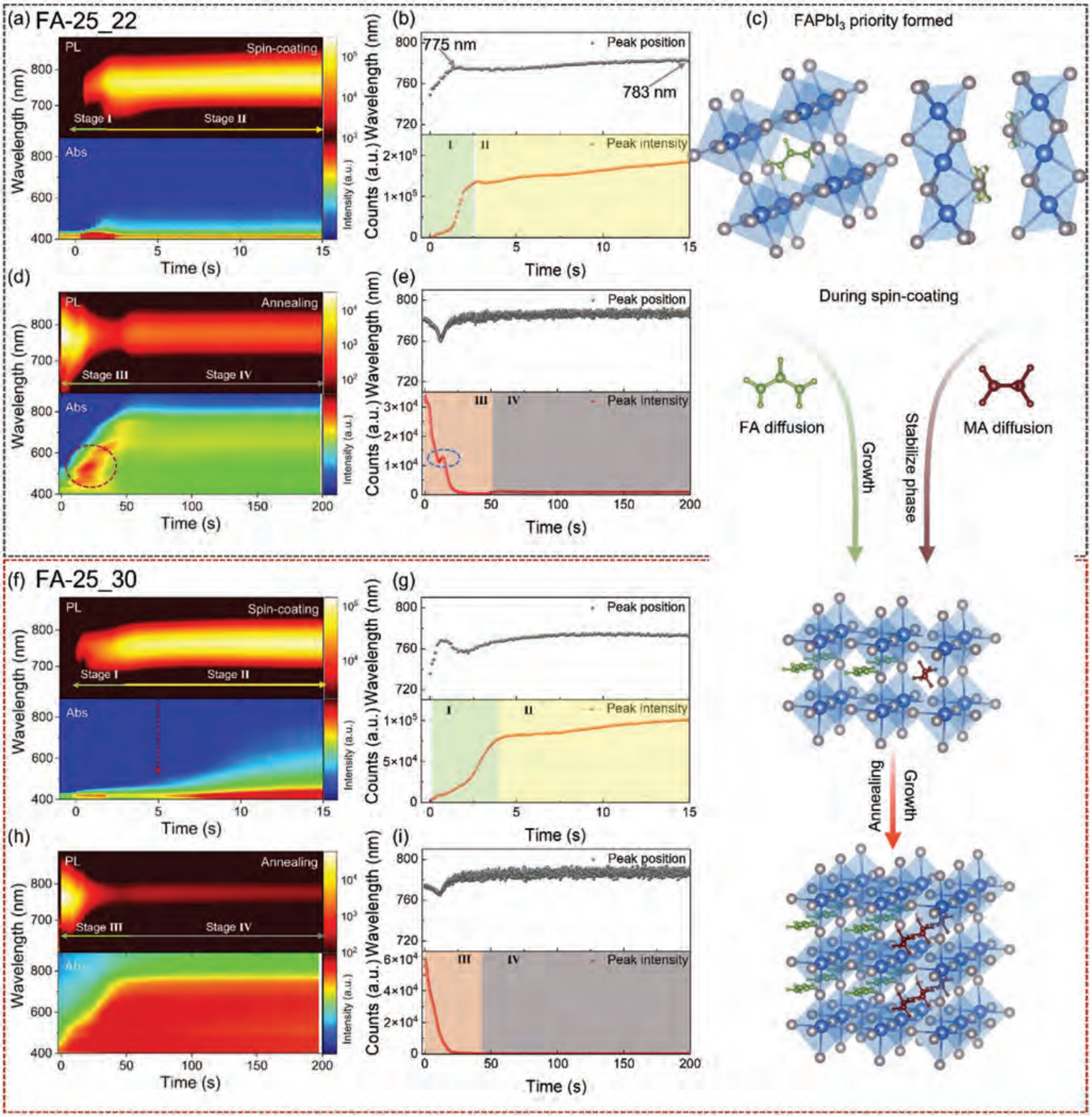

Figure 3. The in situ PL and absorption evolution of FA-25 prepared at an ambient temperature of 22 °C during a) spin-coating and d) annealing. The extracted evolution of PL peak position and intensity by Gaussian fitting during b) spin-coating and e) annealing. c) The schematic diagram of the FA-25 crystallization process. The in situ PL and absorption evolution of FA-25 prepared at an ambient temperature of 30 °C during f) spin-coating and h) annealing. The extracted evolution of PL peak position and intensity by Gaussian fitting during g) spin-coating and i) annealing.

the in situ absorption result that the band-edge absorption starts immediately right after dropping the antisolvent. Consequently, due to the solute depletion induced by nuclei aggregation, there are also a lot of cracks developed in the as-cast FA-50_30 film, as shown in Figure 1b. Similar to the case in FA-25_30, the in situ PL results in FA-50_30 also show little secondary nucleation at the beginning of the thermal annealing. Meanwhile, a smaller blue shift of the PL peak position is observed in FA-50_30 as compared to that in the FA-25_30 film. This is due to the fact that FA-50_30 has fewer MA ions to be incorporated into the lattice during the thermal annealing.

From the above results, it can be safely concluded that the nucleation and crystallization of the precursor materials during the spin-coating play significant roles in determining the perovskite

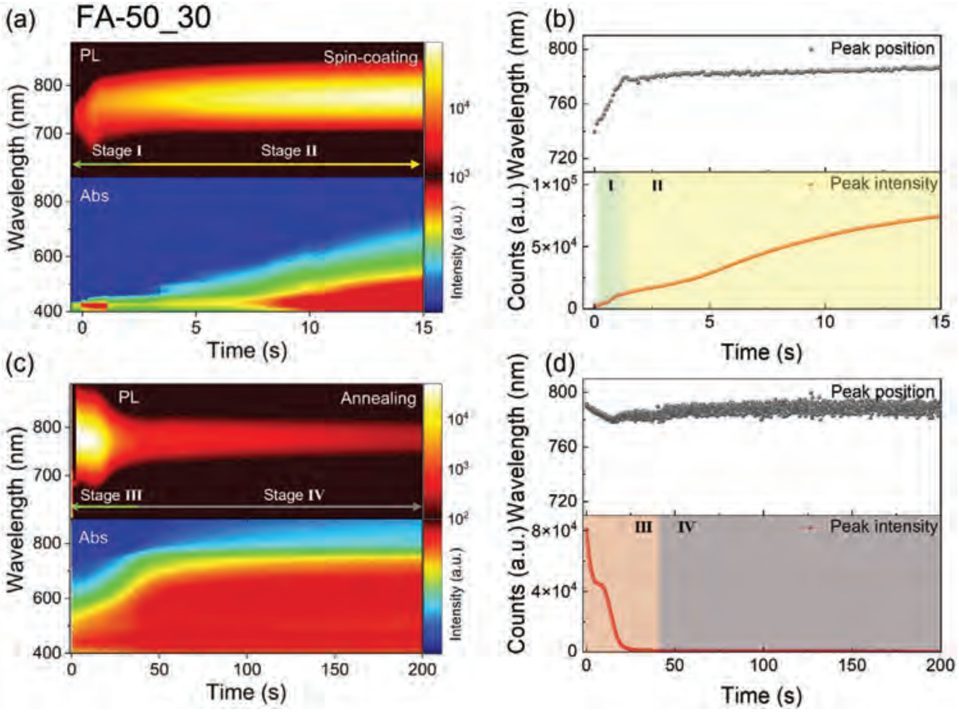

Figure 4. The in situ PL and absorption evolution of FA-50 prepared at an ambient temperature of 30 °C during a) spin-coating and c) annealing. The extracted evolution of PL peak position and intensity by Gaussian fitting during b) spin-coating and d) annealing.

film quality. Particularly, for FA-based perovskites, increasing the processing temperature or the FA content will reduce the amount of solvent incorporated intermediate phase. This facilitates nuclei aggregation and induces solute depletion in the wet perovskite film, deteriorating the film morphology. This crystallization process deduced from the in situ measurement is further supported by the DFT calculation results, as shown in **Figure 5**. Details of the calculation procedures are depicted in the Experimental Section. The formation energy of the DMSO–MA adduct (−2.56 eV) is much lower than that in $MAPbI_3$ (0.12 eV). Therefore, in pure $MAPbI_3$, the $MAPbI_3$ nuclei formed upon the dropping of the antisolvent can be readily redissolved to form the DMSO–MA adducts as observed in the in situ results. On the other hand, in pure $FAPbI_3$, since the formation energy of the DMSO–FA (−1.97 eV) and $FAPbI_3$ (−1.98 eV) are comparable, more $FAPbI_3$ nuclei can be stabilized during the spin-coating, and later being converted to the more stable δ-phase. In the mixed $FAMAPbI_3$, the MA cations not only can stabilize the nuclei but also form DMSO–MA adducts as it has the lower formation energy. The DMSO–MA along with the residual solvent helps to separate the nuclei and prevent the nuclei from aggregation.

The success of perovskites in the photovoltaic market is not only dependent on the device performance, but also the viability in large-scale production. It is well known that the quality of the perovskite film is highly sensitive to the processing conditions, as demonstrated here with the FA-based perovskites. Achieving high-quality FA-based perovskite films requires cooling down the processing environment, especially in the summer. It limits the processing window and increases the energy payback time. Based on the above findings, it is suggested that replacing with another

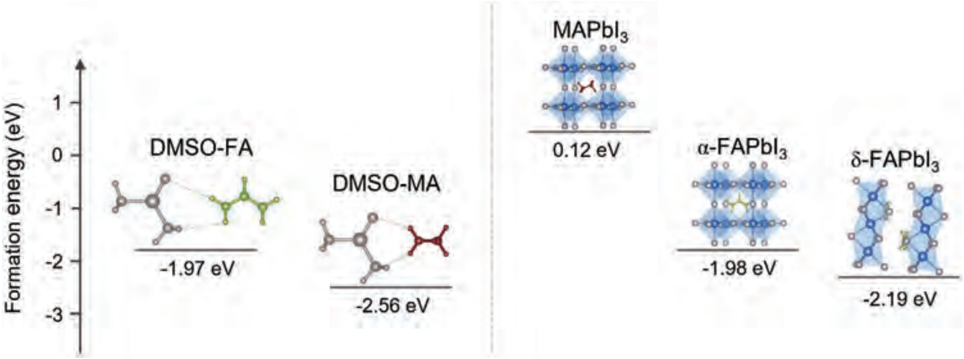

Figure 5. The formation energy of perovskites and solvent-perovskite adducts.

suitable solvent can possibly retard the solvent evaporation during the spin-coating and prevent the nuclei from aggregation. Therefore, it is suggested that a solvent which has a higher boiling point and Gutmann's donor number could resolve the issue of temperature effect in FA-based perovskite. The higher boiling point can lower the solvent evaporation rate, and the higher Gutmann's donor number can facilitate the formation of the solvent adduct.[23] As shown in Figure S23 of the Supporting Information, another solvent NMP, which although has a higher boiling point than that in DMSO, its low Gutmann's donor number eventually increases the crystallization rate of the perovskite film.

3. Conclusion

To conclude, we employed an in situ optical technique to investigate the ambient temperature effect on the $FAMAPbI_3$ perovskite film formation. We have demonstrated that the $FAMAPbI_3$ film morphology and the device performance are highly sensitive to ambient temperature, and a large number of cracks are formed during the spin-coating at around room temperature. Using the in situ technique, we have found that crystallization processes are strikingly different between MA-based and FA-based perovskites. MA-based perovskite trends to form solvent coordinated intermediate phase during the spin-coating. On the other hand, no intermediate phase is formed in FA-based perovskites, and the nucleation trends to be completed. However, we have found that the high density of nuclei in FA-base perovskite induces nuclei aggregation, especially at a higher ambient temperature and in higher FA content. Eventually, the nuclei aggregation induces solute depletion in certain regions in the as-casted perovskite film, leading to the formation of cracks as widely observed in FA-based perovskites. This work demonstrates that the in situ optical method not only can effectively dissect the fast nucleation and crystallization processes in perovskite during the fabrication, but also bring insight into the development of high-quality perovskite film in future large-scale production.

4. Experimental Section

Materials: Tin oxide (SnO_2) colloid precursor (15% in H_2O colloidal dispersion) was purchased from Alfa Aesar. DMF, DMSO, chlorobenzene (CB), and acetonitrile were purchased from Sigma-Aldrich. MAI and FAI were purchased from GreatCell Solar. PbI_2 (99%), 4-tert-butylpyridine, bis (trifluoromethane) sulfonimide lithium salt, phenethylammonium iodide (PEAI), and spiro-OMeTAD were purchased from Xi'an Polymer Light Technology Corp. ITO glass was purchased from Suzhou Shang Yang Solar Technology Company. All the chemical materials were used as received unless stated otherwise.

$FA_xMA_{1-x}PbI_3$ Film Fabrication: MAI (270.2 mg) and PbI_2 (783.7 mg) were dissolved in 1 mL mixture solvent (850 mL DMF and 150 DMSO) for the $MAPbI_3$ precursor. For the $FAPbI_3$ precursor, FAI (292.3 mg) and PbI_2 (783.7 mg) were used. For the $FA_{0.25}MA_{0.75}PbI_3$ precursor, FAI (73.1 mg), MAI (202.6 mg), and PbI_2 (783.7 mg) were used. For the $FA_{0.5}MA_{0.5}PbI_3$ precursor, FAI (135.1 mg), MAI (146.1 mg), and PbI_2 (783.7 mg) were used. For the $FA_{0.75}MA_{0.5}PbI_2$ precursor, FAI (219.3 mg), MAI (67.6 mg), and PbI_2 (783.7 mg) were used. Prior to the film fabrication, the glovebox was purged for several minutes by N_2 to minimize the impact of residual solvent-vapor. The $FA_xMA_{1-x}PbI_3$ precursor solution was spin-coated on the glass substrate at 5000 rpm for 30 s, and 200 µL of CB was dropped on the spinning film 5 s prior to the end of spin-coating. The substrate was then immediately annealed at 120 °C for 40 min.

Device Fabrication: The patterned ITO substrates were sequentially cleaned by detergent, deionized water, ethanol, and finally dried by nitrogen gas. Then, cleaned ITO substrates were treated in an ultraviolet-ozone (UVO) chamber for 10 min. The SnO_2 precursor was spin-coated on the cleaned substrate at 4000 rpm for 30 s and then annealed at 180 °C for 20 min to form the electron transport layer. The SnO_2-coated substrates were further UVO treated before transferring into a glovebox for follow-up procedures. The $MAPbI_3$ and $FA_{0.25}MA_{0.75}PbI_3$ perovskite precursor solution were spin-coated on the SnO_2 layer at 5000 rpm for 30 s, and 200 µL of CB was dropped on the spinning film 5 s prior to the end of spin-coating. The substrates were then immediately annealed at 120 °C for 40 min. Afterward, the PEAI precursor was spin-coated on the perovskite layer at 3000 rpm for 30 s. Then, the spiro-OMeTAD precursor was spin-coated on perovskite film at 4000 rpm for 30 s to form the hole transport layer (HTL). Finally, an Au electrode was evaporated on the HTL with a thickness of 80 nm. The active area of the PSCs was 0.09 cm^2. In addition, the ambient temperature of the glovebox was adjusted by a water-cooling system.

Characterization: The XRD measurements were conducted by a D2 Phaser instrument using Cu Kα ($\lambda = 0.154$ nm) radiation to investigate the crystal structure of perovskites. UV–vis absorption spectra were performed on a Perkin Elmer Lambda 2S UV–vis spectrometer. The PL imaging was measured by WITec alpha300 R Raman System. The AFM images of perovskite films were obtained by Bruker MultiMode 8-HR AFM System. The SEM was conducted by electron microscope scanning (QUATTRO S). The *J–V* curves were measured by a Keithley 2400 source meter unit under AM 1.5G illustration at 100 mW cm^{-2} with a standard silicon solar cell (certified by NREL). The EQE spectrum was measured by a solar cell spectral response measurement system (QER3-011, Enli Technology Co. Ltd., Taiwan). The in situ optical techniques were set inside a temperature-controlled nitrogen-filled glovebox. The laser intensity was maintained at 8 mW cm^{-2}. In the in situ test, specialized spin-coating holder and hotplate were adopted to avoid background noise PL signal, as shown in Figure S12 of the Supporting Information. The same setup was also used to conduct an in situ absorption test by replacing the laser light source with a halogen lamp, and the spectrum of the light source is shown in Figure S24 of the Supporting Information. Detailed information on in situ optical technique is shown in Figures S11–S13 of the Supporting Information. The temperature evolution of substrate placed on the 120 °C hotplate is given by the infrared camera (Optris PI 400i).

DFT Calculation: The DFT calculations were performed using Vienna Ab initio Simulation Package code with the full-potential projected augmented wave formalism.[24] The generalized gradient approximation of the Perdew–Burke–Ernzerhof functional was used to describe the exchange and correlation functional.[25] The cut-off energy for the plane-wave expansion was set to 450 eV, and a k-point mesh of $5 \times 5 \times 5$ was employed to sample the Brillouin zone of the unit cell. In structural relaxation, the structure was relaxed until the maximum stress on each atom was lower than 0.01 eV Å^{-1}. In the energy calculation, a convergence criterion of 10^{-4} eV was set for self-consistence.

Supporting Information

Supporting Information is available from the Wiley Online Library or from the author.

Acknowledgements

The authors acknowledge the General Research Fund (CityU 11304420 and 11317420) from the Research Grants Council of Hong Kong S.A.R., China. S.-W.T. acknowledges helpful discussions with Prof. C. H. Shek on the crystallization process studied in this work.

Conflict of Interest

The authors declare no conflict of interest.

Data Availability Statement

Research data are not shared.

Keywords

crystallization, in situ optical method, multiple cation-composited perovskites, nucleation

Received: July 31, 2023
Revised: September 6, 2023

[1] a) J.-W. Lee, S. Tan, S. I. Seok, Y. Yang, N.-G. Park, *Science* **2022**, *375*, 1186; b) A. Binek, F. C. Hanusch, P. Docampo, T. Bein, *J. Phys. Chem. Lett.* **2015**, *6*, 1249; c) N. J. Jeon, J. H. Noh, W. S. Yang, Y. C. Kim, S. Ryu, J. Seo, S. I. Seok, *Nature* **2015**, *517*, 476; d) D. J. Kubicki, D. Prochowicz, A. Hofstetter, P. Péchy, S. M. Zakeeruddin, M. Grätzel, L. Emsley, *J. Am. Chem. Soc.* **2017**, *139*, 10055; e) D. J. Kubicki, D. Prochowicz, A. Hofstetter, M. Saski, P. Yadav, D. Bi, N. Pellet, J. Lewinski, S. M. Zakeeruddin, M. Grätzel, L. Emsley, *J. Am. Chem. Soc.* **2018**, *140*, 3345; f) B.-W. Park, S. I. Seok, *Adv. Mater.* **2019**, *31*, 1805337; g) H. Lu, Y. Liu, P. Ahlawat, A. Mishra, W. R. Tress, F. T. Eickemeyer, Y. Yang, F. Fu, Z. Wang, C. E. Avalos, B. I. Carlsen, A. Agarwalla, X. Zhang, X. Li, Y. Zhan, S. M. Zakeeruddin, L. Emsley, U. Rothlisberger, L. Zheng, A. Hagfeldt, M. Gratzel, *Science* **2020**, *370*; h) J. V. Milic, S. M. Zakeeruddin, M. Grätzel, *Acc. Chem. Res.* **2021**, *54*, 2729; i) Y. Wang, P. Xiang, A. Ren, H. Lai, Z. Zhang, Z. Xuan, Z. Wan, J. Zhang, X. Hao, L. Wu, *ACS Appl. Mater. Interfaces* **2020**, *12*, 53973.

[2] a) M. Yang, Z. Li, M. O. Reese, O. G. Reid, D. H. Kim, S. Siol, T. R. Klein, Y. Yan, J. J. Berry, M. F. Van Hest, *Nat. Energy* **2017**, *2*, 17038; b) H. Chen, F. Ye, W. Tang, J. He, M. Yin, Y. Wang, F. Xie, E. Bi, X. Yang, M. Grätzel, L. Han, *Nature* **2017**, *550*, 92; c) E. H. Jung, N. J. Jeon, E. Y. Park, C. S. Moon, T. J. Shin, T.-Y. Yang, J. H. Noh, J. Seo, *Nature* **2019**, *567*, 511; d) G. Tong, D.-Y. Son, L. K. Ono, Y. Liu, Y. Hu, H. Zhang, A. Jamshaid, L. Qiu, Z. Liu, Y. Qi, *Adv. Energy Mater.* **2021**, *11*, 2003712.

[3] a) A. Thote, I. Jeon, J.-W. Lee, S. Seo, H.-S. Lin, Y. Yang, H. Daiguji, S. Maruyama, Y. Matsuo, *ACS Appl. Energy Mater.* **2019**, *2*, 2486; b) P. Wang, Q. Jiang, Y. Zhao, Y. Chen, Z. Chu, X. Zhang, Y. Zhou, J. You, *Kexue Tongbao (Foreign Lang. Ed.)* **2018**, *63*, 726.

[4] a) A. Kojima, K. Teshima, Y. Shirai, T. Miyasaka, *J. Am. Chem. Soc.* **2009**, *131*, 6050; b) M. Kim, J. Jeong, H. Lu, T. K. Lee, F. T. Eickemeyer, Y. Liu, I. W. Choi, S. J. Choi, Y. Jo, H.-B. Kim, S.-I. Mo, Y.-K. Kim, H. Lee, N. G. An, S. Cho, W. R. Tress, S. M. Zakeeruddin, A. Hagfeldt, J. Y. Kim, M. Grätzel, D. S. Kim, *Science* **2022**, *375*, 302; c) S. Zhan, Y. Duan, Z. Liu, L. Yang, K. He, Y. Che, W. Zhao, Y. Han, S. Yang, G. Zhao, *Adv. Energy Mater.* **2022**, *12*, 2200867; d) H. Min, D. Y. Lee, J. Kim, G. Kim, K. S. Lee, J. Kim, M. J. Paik, Y. K. Kim, K. S. Kim, M. G. Kim, T. J. Shin, S. Il Seok, *Nature* **2021**, *598*, 444.

[5] a) X. Zheng, C. Wu, S. K. Jha, Z. Li, K. Zhu, S. Priya, *ACS Energy Lett.* **2016**, *1*, 1014; b) T. Liu, Y. Zong, Y. Zhou, M. Yang, Z. Li, O. S. Game, K. Zhu, R. Zhu, Q. Gong, N. P. Padture, *Chem. Mater.* **2017**, *29*, 3246; c) Q. Hu, L. Zhao, J. Wu, K. Gao, D. Luo, Y. Jiang, Z. Zhang, C. Zhu, E. Schaible, A. Hexemer, C. Wang, Y. Liu, W. Zhang, M. Grätzel, F. Liu, T. P. Russell, R. Zhu, Q. Gong, *Nat. Commun.* **2017**, *8*, 15688.

[6] a) A. D. Taylor, Q. Sun, K. P. Goetz, Q. An, T. Schramm, Y. Hofstetter, M. Litterst, F. Paulus, Y. Vaynzof, *Nat. Commun.* **2021**, *12*, 1878; b) N. J. Jeon, J. H. Noh, Y. C. Kim, W. S. Yang, S. Ryu, S. I. Seok, *Nat. Mater.* **2014**, *13*, 897; c) Y. Fang, T. Tian, M. Yang, Y. Tan, J.-X. Zhong, Y. Huang, X. Wang, J. Tao, S. Yang, C. Zou, S. Yang, Y. Peng, Q. Xue, W.-Q. Wu, *Adv. Funct. Mater.* **2023**, *33*, 2303674.

[7] M. Saliba, J.-P. Correa-Baena, C. M. Wolff, M. Stolterfoht, N. Phung, S. Albrecht, D. Neher, A. Abate, *Chem. Mater.* **2018**, *30*, 4193.

[8] J. Ye, G. Liu, L. Jiang, H. Zheng, L. Zhu, X. Zhang, H. Wang, X. Pan, S. Dai, *Appl. Surf. Sci.* **2017**, *407*, 427.

[9] H. B. Lee, M. K. Jeon, N. Kumar, B. Tyagi, J. W. Kang, *Adv. Funct. Mater.* **2019**, *29*, 1903213.

[10] N. Li, X. Niu, L. Li, H. Wang, Z. Huang, Y. Zhang, Y. Chen, X. Zhang, C. Zhu, H. Zai, Y. Bai, S. Ma, H. Liu, X. Liu, Z. Guo, G. Liu, R. Fan, H. Chen, J. Wang, Y. Lun, X. Wang, J. Hong, H. Xie, D. S. Jakob, X. G. Xu, Q. Chen, H. Zhou, *Science* **2021**, *373*, 561.

[11] W. Feng, J. Tao, G. Liu, G. Yang, J.-X. Zhong, Y. Fang, L. Gong, S. Yang, W.-Q. Wu, *Angew. Chem.* **2023**, *135*, 202300265.

[12] a) J. Wang, Z. Gao, J. Yang, M. Lv, H. Chen, D. J. Xue, X. Meng, S. Yang, *Adv. Energy Mater.* **2021**, *11*, 2102131; b) W. Xiang, J. Zhang, S. Liu, S. Albrecht, A. Hagfeldt, Z. Wang, *Joule* **2022**, *6*, 315; c) J. Ma, M. Qin, Y. Li, X. Wu, Z. Qin, Y. Wu, G. Fang, X. Lu, *Matter* **2021**, *4*, 313; d) B. Li, D. Binks, G. Cao, J. Tian, *Small* **2019**, *15*, 1903613.

[13] a) M. Kim, G.-H. Kim, T. K. Lee, I. W. Choi, H. W. Choi, Y. Jo, Y. J. Yoon, J. W. Kim, J. Lee, D. Huh, H. Lee, S. K. Kwak, J. Y. Kim, D. S. Kim, *Joule* **2019**, *3*, 2179; b) M. Wang, B. Li, P. Siffalovic, L.-C. Chen, G. Cao, J. Tian, *J. Mater. Chem. A* **2018**, *6*, 15386.

[14] a) L. Cai, C. W. Suen, Y. S. Lau, Z. Lan, J. Han, F. Zhu, *ACS Appl. Energy Mater.* **2022**, *5*, 8304; b) D. Liu, D. Luo, A. N. Iqbal, K. W. P. Orr, T. A. S. Doherty, Z.-H. Lu, S. D. Stranks, W. Zhang, *Nat. Mater.* **2021**, *20*, 1337.

[15] a) M. Shirayama, H. Kadowaki, T. Miyadera, T. Sugita, M. Tamakoshi, M. Kato, T. Fujiseki, D. Murata, S. Hara, T. N. Murakami, S. Fujimoto, M. Chikamatsu, H. Fujiwara, *Phys. Rev. Appl.* **2016**, *5*, 014012; b) L. Wagner, L. E. Mundt, G. Mathiazhagan, M. Mundus, M. C. Schubert, S. Mastroianni, U. Würfel, A. Hinsch, S. W. Glunz, *Sci. Rep.* **2017**, *7*, 14899; c) E. S. Parrott, J. B. Patel, A.-A. Haghighirad, H. J. Snaith, M. B. Johnston, L. M. Herz, *Nanoscale* **2019**, *11*, 14276; d) M. Li, R. Begum, J. Fu, Q. Xu, T. M. Koh, S. A. Veldhuis, M. Grätzel, N. Mathews, S. Mhaisalkar, T. C. Sum, *Nat. Commun.* **2018**, *9*, 4197.

[16] S. Pratap, F. Babbe, N. S. Barchi, Z. Yuan, T. Luong, Z. Haber, T.-B. Song, J. L. Slack, C. V. Stan, N. Tamura, C. M. Sutter-Fella, P. Müller-Buschbaum, *Nat. Commun.* **2021**, *12*, 5624.

[17] a) S. Sánchez, L. Pfeifer, N. Vlachopoulos, A. Hagfeldt, *Chem. Soc. Rev.* **2021**, *50*, 7108; b) C. Liu, Y.-B. Cheng, Z. Ge, *Chem. Soc. Rev.* **2020**, *49*, 1653.

[18] a) T. Huang, S. Tan, S. Nuryyeva, I. Yavuz, F. Babbe, Y. Zhao, M. Abdelsamie, M. H. Weber, R. Wang, K. N. Houk, C. M. Sutter-Fella, Y. Yang, *Sci. Adv.* **2021**, *7*, 1799; b) K. Suchan, J. Just, P. Becker, E. L. Unger, T. Unold, *J. Mater. Chem. A* **2020**, *8*, 10439.

[19] T. Yang, L. Gao, J. Lu, C. Ma, Y. Du, P. Wang, Z. Ding, S. Wang, P. Xu, D. Liu, H. Li, X. Chang, J. Fang, W. Tian, Y. Yang, S. Liu, K. Zhao, *Nat. Commun.* **2023**, *14*, 839.

[20] a) J. Zhang, X. Jiang, X. Liu, X. Guo, C. Li, *Adv. Funct. Mater.* **2022**, *32*, 2204642; b) X. Chen, Y. Xia, Z. Zheng, X. Xiao, C. Ling, M. Xia, Y. Hu, A. Mei, R. Cheacharoen, Y. Rong, H. Han, *Chem. Mater.* **2022**, *34*, 728; c) L. Chen, J. W. Yoo, M. Hu, S.-U. Lee, S. I. Seok, *Angew. Chem., Int. Ed.* **2022**, *61*, 202212700; d) D. Yao, C. Zhang, N. D. Pham, Y. Zhang, V. T. Tiong, A. Du, Q. Shen, G. J. Wilson, H. Wang, *J. Phys. Chem. Lett.* **2018**, *9*, 2113.

[21] L. Bi, Q. Fu, Z. Zeng, Y. Wang, F. R. Lin, Y. Cheng, H.-L. Yip, S. W. Tsang, A. K.-Y. Jen, *J. Am. Chem. Soc.* **2023**, *145*, 5920.

[22] S. Wu, H. S. Soreide, B. Chen, J. Bian, C. Yang, C. Li, P. Zhang, P. Cheng, J. Zhang, Y. Peng, G. Liu, Y. Li, H. J. Roven, J. Sun, *Nat. Commun.* **2022**, *13*, 3495.

[23] D. Angmo, X. Peng, A. Seeber, C. Zuo, M. Gao, Q. Hou, J. Yuan, Q. Zhang, Y.-B. Cheng, D. Vak, *Small* **2019**, *15*, 1904422.

[24] a) G. Kresse, J. Furthmüller, *Phys. Rev. B* **1996**, *54*, 11169; b) P. E. Blöchl, *Phys. Rev. B* **1994**, *50*, 17953.

[25] J. P. Perdew, K. Burke, M. Ernzerhof, *Phys. Rev. Lett.* **1996**, *77*, 3865.

[26] A. He, Y. Wang, P. Tang, Z. Zhang, Z. Zeng, Y. Zhang, X. Hao, L. Wu, S. K. So, S. Tsang, J. Zhang, *Adv. Energy Mater.* **2023**, https://doi.org/10.1002/aenm.202300957.

[27] J.-W. Lee, S. Tan, S. I. Seok, Y. Yang, N.-G. Park, *Science* **2022**, *375*, https://doi.org/10.1126/science.abj1186.

[28] A. Binek, F. C. Hanusch, P. Docampo, T. Bein, *J. Phys. Chem. Lett.* **2015**, *6*, 1249.

[29] N. J. Jeon, J. H. Noh, W. S. Yang, Y. C. Kim, S. Ryu, J. Seo, S. I. Seok, *Nature* **2015**, *517*, 476.

[30] D. J. Kubicki, D. Prochowicz, A. Hofstetter, P. Péchy, S. M. Zakeeruddin, M. Grätzel, L. Emsley, *J. Am. Chem. Soc.* **2017**, *139*, 10055.

[31] B. Park, S. I. Seok, *Adv. Mater.* **2015**, *31*, https://doi.org/10.1002/adma.201805337.

[32] H. Lu, Y. Liu, P. Ahlawat, A. Mishra, W. R. Tress, F. T. Eickemeyer, Y. Yang, F. Fu, Z. Wang, C. E. Avalos, B. I. Carlsen, A. Agarwalla, X. Zhang, X. Li, Y. Zhan, S. M. Zakeeruddin, L. Emsley, U. Rothlisberger, L. Zheng, M. Grätzel, *Science* **2020**, *370*, https://doi.org/10.1126/science.abb8985.

[33] Y. Wang, P. Xiang, A. Ren, H. Lai, Z. Zhang, Z. Xuan, Z. Wan, J. Zhang, X. Hao, L. Wu, M. Sugiyama, U. Schwingenschlögl, C. Liu, Z. Tang, J. Wu, Z. Wang, D. Zhao, *ACS Appl. Mater. Interfaces* **2020**, *12*, 53973.

[34] Y. Yang, M. Yang, D. T. Moore, Y. Yan, E. M. Miller, K. Zhu, M. C. Beard, *Nat. Energy* **2017**, *2*, https://doi.org/10.1038/nenergy.2016.207.

[35] H. Chen, F. Ye, W. Tang, J. He, M. Yin, Y. Wang, F. Xie, E. Bi, X. Yang, M. Grätzel, L. Han, *Nature* **2017**, *550*, 92.

[36] E. H. Jung, N. J. Jeon, E. Y. Park, C. S. Moon, T. J. Shin, T.-Y. Yang, J. H. Noh, J. Seo, *Nature* **2019**, *567*, 511.

[37] G. Tong, D. Son, L. K. Ono, Y. Liu, Y. Hu, H. Zhang, A. Jamshaid, L. Qiu, Z. Liu, Y. Qi, *Adv. Energy Mater.* **2021**, *11*, https://doi.org/10.1002/aenm.202003712.

[38] Z. Zhang, Y. Tang, Y. Wang, Z. Zeng, R. Shi, H. Yan, S.-W. Tsang, C. Cheng, S. K. So, *ACS Appl. Mater. Interfaces* **2022**, *14*, 30174.